Geophys. J. Int. (2007) **169,** 1366–1375 doi: 10.1111/j.1365-246X.2007.03426.x

Simulation of diagenesis and permeability variation in two-dimensional rock structure

S. Sadhukhan,[1] T. Dutta[2] and S. Tarafdar[1]

[1]*Condensed Matter Physics Research Centre, Physics Department, Jadavpur University, Kolkata* 700032*, India. E-mail: sujata_tarafdar@hotmail.com*
[2]*Physics Department, St. Xavier's College, Kolkata* 700016*, India*

Accepted 2007 March 1. Received 2006 September 25; in original form 2006 April 7

SUMMARY

A model is suggested to simulate the physical aspect of diagenesis in porous rocks. A bidisperse ballistic deposition model with relaxation of deposited grains is used to generate the porous structure. Sedimentation and erosion are allowed to restructure the pore space as a fluid flows through the rock. The effect of this restructuring of the pore space on permeability is studied. The Navier–Stokes equation is solved numerically by the finite difference method to determine the pressure and velocity distributions in the pore space. We find that though deposition is the dominant process in our model of diagenesis, reducing the porosity, the permeability may increase dramatically in some cases. These are when the erosion takes place at a single narrow constriction in the pore channel.

Key words: diagenesis, permeability, porous medium, sedimentary rock.

1 INTRODUCTION

The process of 'diagenesis', restructures sedimentary rocks after the initial process of sand deposition. This affects dynamic properties of electrical and fluid transport through the pore network. Generating a realistic porous rock structure by a simple computer algorithm is itself a challenging problem. Much work has been done in this direction (Dasgupta *et al*. 2000; Dutta & Tarafdar 2003; Manwart *et al*. 2000; Øren & Bakke 2003; Pape *et al*. 1999; Schwartz *et al*. 1993). After creating a porous structure, one studies its properties, such as porosity, permeability to fluid flow and electrical conductivity, when the pores are filled with conducting brine. When real rocks are formed, the geological process of diagenesis (Pettijohn 1984) leads to erosion as well as formation of mineral deposits or cementation, which gradually change the pore structure and hence, porosity and permeability.

Real rocks are 3-D structures with highly tortuous and often fractal pore spaces. Before attempting simulation of this daunting geometry, we present here, as a preliminary study a simpler 2-D version. We generate a porous stochastic structure in 2-D and simulate flow of a single fluid through it, using a numerical finite difference solution of the steady state Navier–Stokes equation. Next, we introduce a simplified algorithm to mimic diagenesis, which deposits solid material at low- fluid velocity regions and erodes the solid rock, where velocity is high. This changes details of the pore channel and results in a change in permeability. While this may not be an entirely faithful representation of the true situation, it gives an idea of changes, which may occur at the submacroscopic level and can be a first step towards tackling the 3-D problem in all its complexity. Our present treatment of diagenesis does not take into account molecular diffusion or details of chemical reactions occurring during diagenesis. These may be introduced in future extensions of the model.

Our study shows that simulation of diagenesis by the present algorithm with net deposition dominating over erosion, leads interestingly to an overall increase in permeability. We discuss the reason behind this seemingly paradoxical result on the basis of the details of restructuring of the pore channel.

Our results are seemingly in conflict with the general belief that permeability necessarily decreases with porosity. This effect is not a result of the flow itself shaping the pore channel, as in our model. Molecular diffusion and compaction with grains being crushed are probably responsible for permeability reduction with porosity.

2 CREATING THE ROCK STRUCTURE AND FLOW CHANNELS

We follow the procedure discussed in (Dutta & Tarafdar 2005) to generate a porous structure with a connected rock phase. Under appropriate conditions, the pore phase is also connected. We refer to this model as the Relaxed Bidisperse Ballistic Deposition Model (RBBDM).

The basic algorithm is to deposit particles of two different sizes ballistically. In 2-D (1 + 1 model), we drop square 1×1 and elongated 2×1 'grains' on a linear substrate. The square grains are chosen with a probability p and elongated grains with probability $(1-p)$. The presence of the longer grains leads to gaps in the structure. The porosity Φ, defined as the vacant fraction of the total volume (area in 2-D) depends on the value of p. Variation of Φ with p follows a logarithmic law as discussed in Dasgupta *et al*., (2000); Tarafdar & Roy (1998). For very high p, the pores are isolated, but as p decreases, pores spanning the sample start to appear. It was shown that in 3-D, the sample spanning pores are fractal (Dutta & Tarafdar 2003). This is the basic BBDM, without relaxation, studied by Dasgupta *et al*. (2000); Dutta & Tarafdar (2003); Tarafdar &

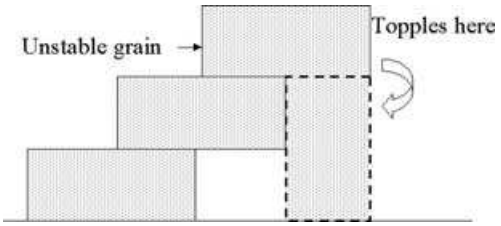

Figure 1. The rule for deposition and toppling of an unstable grain to a relaxed position in RBBDM is illustrated. The broken outline shows the position the topmost large grain relaxes to.

Roy (1998). In the RBBDM, a relaxation of the grains deposited in an unstable position is introduced in Dutta & Tarafdar (2005). This accounts partially for the compaction during growth of sedimentary rocks.

The elongated grains are deposited with their long axis horizontal. If a larger particle settles on a smaller particle, a one step overhang is created if there is no particle immediately below the protruding end of the larger particle. If a second larger particle settles midway on the previous large particle, a two-step overhang is created, if there is no supporting particle immediately below the protrusion of the second overhang. This two-step overhang is not stable and the second large particle topples over if possible, according to the scheme shown in Fig. 1.

The relaxation obviously decreases the porosity and in RBBDM Φ is maximum for $p = 0.5$. The configuration average of this value is $\varphi = 0.3635$, whereas for the unrelaxed BBDM, Φ decreases monotonically with p.

In the present 2-D model, it is obviously impossible to have both rock and pore phases connected in both x- and y- directions. We consider the y- direction as vertical, and thus the solid phase in necessarily connected in this direction. For fluid flow, we look for pore channels spanning the sample in the y-direction.

The simulation procedure is described in detail in Dasgupta *et al*. (2000); Dutta & Tarafdar (2003); Dutta & Tarafdar (2005); Tarafdar & Roy (1998). Here, we show the nature of the 2-D pore structure in Figs. 2a and 2b, for different p.

The maximum porosity attained here is below the percolation threshold in 2-D for random percolation (Stauffer & Aharony 1994). Though the present algorithm is different from random percolation, we may expect most of the configurations generated for finite sizes of about 128×128 to have no pore channel spanning the cluster. We reject those configurations which do not percolate and choose only those where at least one spanning pore exists. The connected channels are identified by the well-known algorithm given by Hoshen & Kopelman 1976. Earlier stochastic models of porous rock structure (Jin *et al*. 2004; Manwart *et al*. 2000; Pape *et al*. 1999.) reproduce successfully the *final* structure. On the other hand, RBBDM attempts to simulate the generation *process* of the rock, leading naturally to a realistic structure.

3 FLUID FLOW IN CONNECTED CHANNELS

We assume that a homogeneous and incompressible Newtonian fluid is flowing through connected channels, similar to those shown in Figs 2(a) and (b). The pressure difference driving the flow may be due to gravity, if we consider our 2-D 'rock' to be vertical. If it is lying in a horizontal plane, the pressure may be supposed to arise from sources other than gravity.

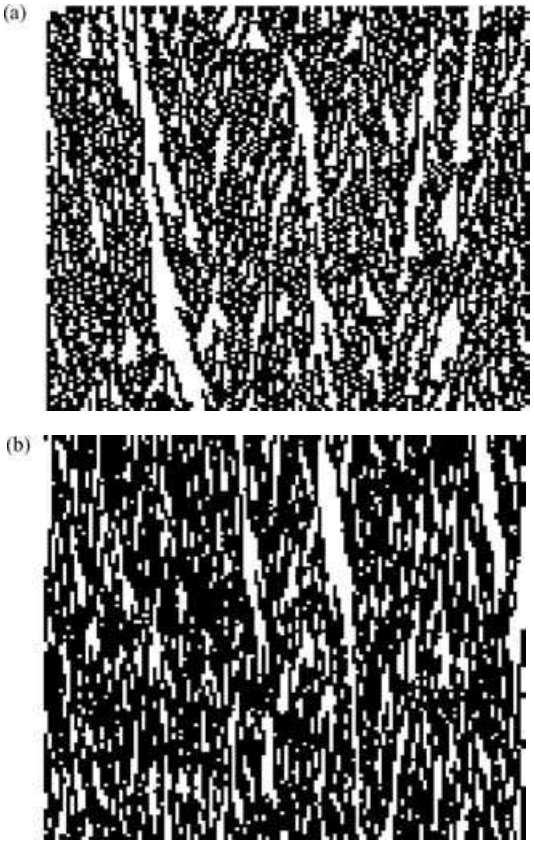

Figure 2. (a) We show the 2-D porous structures generated by RBBDM for the fraction of small grains 'p' $= 0$, with porosity 0.34. The sample is of size 128×128. (b) We show the 2-D porous structures generated by RBBDM for the fraction of small grains 'p' $= 0.9$, with porosity 0.25. The sample is of size 128×128.

In order to apply the finite difference method for numerical solution described below, it is necessary for the minimum width of the pore channel to be at least 3 units in terms of the smallest unit of resolution. This is because, with no-slip boundary conditions, the 2 sites (or cells), adjacent to the walls of the pore have zero velocity, so to have a finite flow, there must be a third cell between these 2, having non-zero velocity. Increasing this number from 3, as much as practicable will generate the true parabolic velocity profile. However, in view of limited computer time and memory, we have at present restricted this minimum number to 4. This means that, each site (either solid or vacant) we have generated by RBBDM, described above, has to be replaced by a 4×4 square grid, increasing the linear size of our sample 4 times. Each of these smaller squares is henceforth our new unit. This ensures that fluid may flow through even the narrowest channel in our system. We are interested in finding the pressure and velocity distribution in the channel. The relevant equations describing the pressure and velocity and the method of numerically solving these is detailed below. We have broadly followed the procedure described by Sarkar *et al*. (2004) with some necessary departures appropriate to our problem.

The equation of motion for such a fluid is given by Navier–Stokes equation.

$$\rho \left[\frac{\partial \vec{V}}{\partial t} + (\vec{V}.\vec{\nabla})\vec{V} \right] + \vec{\nabla} P - \mu \nabla^2 \vec{V} = \vec{f}_e, \tag{1}$$

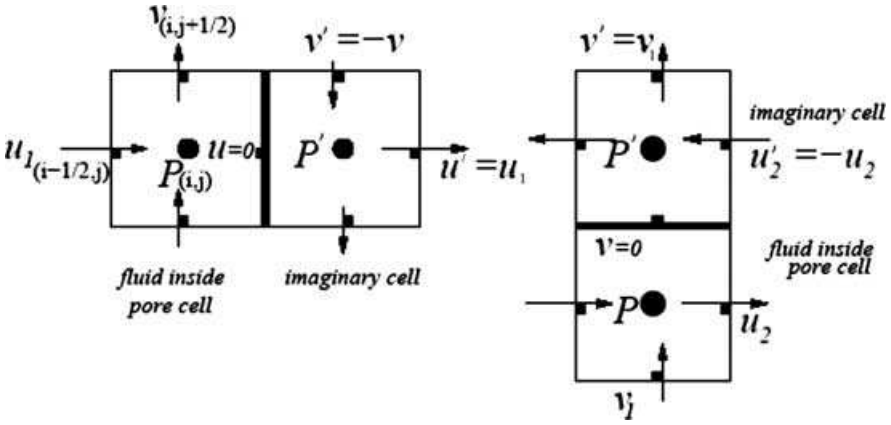

Figure 3. The grid cells for pressure P and velocity components u and v are shown here. The unprimed coordinates represent a vacant site in the real pore space, the heavy black line is the pore–solid interface and the primed quantities represent the pressure and velocity introduced in the image cell to preserve proper boundary conditions described in the text. The figure on the left is for the vertical boundary and the the right-hand side figure is for the horizontal.

where $\vec{V}$ represents the velocity vector, P is the pressure, $\vec{f}_e$ is the external force per unit volume, ρ and μ are the density and the dynamic viscosity of the fluid. We also assume that the fluid flow is slow enough so that the inertial terms $\rho(\vec{V}.\vec{\nabla})\vec{V}$ can be neglected and there are no external forces acting on the fluid. This gives rise to a simplified form of equation (1) known as Stoke's equation.

$$\frac{\partial \vec{V}}{\partial t} = -\frac{1}{\rho}\vec{\nabla}P + \eta\nabla^2\vec{V}, \tag{2}$$

where $\eta = \mu/\rho$ is the kinematic viscosity.

The equation of continuity is represented as

$$\vec{\nabla}.\vec{V} + \frac{\partial \rho}{\partial t} = 0. \tag{3}$$

Since the fluid is incompressible, the second term vanishes resulting in

$$\vec{\nabla}\vec{V} = 0. \tag{4}$$

Equations (2) and (4) are solved numerically, by applying the method of finite difference.

Pressure and scalar component of velocity can be discretized for both space and time through finite difference equations.

Taking discrete time finite difference of eqs. (2) and (4), we get the following

$$\frac{\vec{V^{n+1}} - \vec{V^n}}{\Delta t} = -\frac{1}{\rho}\vec{\nabla}P^{n+1} + \eta\nabla^2\vec{V^{n+1}}, \tag{5}$$

$$\vec{\nabla}\vec{V}^{n+1} = 0. \tag{6}$$

The physical significance of eq. (6) is that the velocity obeys the equation of continuity at an advanced step (n+1), while its change over time from n to (n+1) is computed from eq. (5).

Taking divergence of eq. (5), we get

$$\frac{\vec{\nabla}.\vec{V^{n+1}} - \vec{\nabla}.\vec{V^n}}{\Delta t} = -\frac{1}{\rho}\nabla^2 P^{n+1} + \eta\nabla^2(\vec{\nabla}.\vec{V^{n+1}}). \tag{7}$$

Substituting eq. (6) in (7), we get

$$\nabla^2 P^{n+1} = \frac{\rho}{\Delta t}(\vec{\nabla}.\vec{V^n}). \tag{8}$$

Equation (5) can be rearranged as

$$\vec{V^{n+1}} - \eta\Delta t\nabla^2\vec{V^{n+1}} = \vec{V^n} - \frac{\Delta t}{\rho}\vec{\nabla}P^{n+1}. \tag{9}$$

In our problem, we have applied a pressure gradient between the two ends of the pore channel embedded within the rock. The fluid is assumed to enter through the inlet with an unknown velocity. As it continues to flow through the channel, its motion is determined by the pressure gradient acting on it.

The initial condition is taken as $n = 0$, $\vec{V^n} = \vec{V^0} = 0$. The updated pressure P^{n+1} is computed from eq. (8), which is used in eq. (9) to compute the updated velocity $\vec{V^{n+1}}$. The new velocity $\vec{V^{n+1}}$ is then used as $\vec{V^n}$ and eq. (8) and (9) are iterated till the steady state is reached. Steady- state flow is one in which the velocity vector is independent of time. Numerically, this condition is satisfied when $|V^{n+1} - V^n|_\alpha < \varepsilon$, where ε is a very small quantity, defined by the user depending on the accuracy required. If this condition is satisfied after m iterations then P^m and $\vec{V^m}$ are the steady state solutions for pressure and velocity, respectively.

The pore channel is divided into square grid-cells. P is the pressure at the centre of a grid-cell, u and v are the components of $\vec{V}$ defined on the faces of the grid-cells, such that they are mutually perpendicular as shown in Fig. 3.

Equations (8) and (9) can be represented as the following after applying central finite difference approximation for spatial derivatives of pressure and the velocity components.

Here, Δx is the spatial discretization unit, and in our case, it is equal to the side of the square grid-cells. Hence, $\Delta x = \Delta y$.

$$\frac{P^{n+1}_{i-1,j} - 2P^{n+1}_{i,j} + P^{n+1}_{i+1,j}}{(\Delta x)^2} + \frac{P^{n+1}_{i,j-1} - 2P^{n+1}_{i,j} + P^{n+1}_{i,j+1}}{(\Delta x)^2} = \frac{\rho}{\Delta t}\left[\frac{u^n_{i+\frac{1}{2},j} - u^n_{i-\frac{1}{2},j}}{2\left(\frac{\Delta x}{2}\right)} + \frac{v^n_{i,j+\frac{1}{2}} - v^n_{i,j-\frac{1}{2}}}{2\left(\frac{\Delta x}{2}\right)}\right], \tag{10}$$

$$u^{n+1}_{i+\frac{1}{2},j} - \eta\Delta t\left(\frac{u^{n+1}_{i-\frac{1}{2},j} - 2u^{n+1}_{i+\frac{1}{2},j} + u^{n+1}_{i+\frac{3}{2},j}}{(\Delta x)^2} + \frac{u^{n+1}_{i+\frac{1}{2},j-1} - 2u^{n+1}_{i+\frac{1}{2},j} + u^{n+1}_{i+\frac{1}{2},j+1}}{(\Delta x)^2}\right) = u^n_{i+\frac{1}{2},j} - \frac{\Delta t}{\rho}\left(\frac{P^{n+1}_{i+1,j} - P^{n+!}_{i,j}}{\Delta x}\right), \tag{11}$$

$$v^{n+1}_{i,j-\frac{1}{2}} - \eta\Delta t\left(\frac{v^{n+1}_{i,j-\frac{3}{2}} - 2v^{n+1}_{i,j-\frac{1}{2}} + v^{n+1}_{i,j+\frac{1}{2}}}{(\Delta x)^2} + \frac{v^{n+1}_{i-1,j-\frac{1}{2}} - 2v^{n+1}_{i,j-\frac{1}{2}} + v^{n+1}_{i+1,j-\frac{1}{2}}}{(\Delta x)^2}\right) = v^{n}_{i,j-\frac{1}{2}} - \frac{\Delta t}{\rho}\left(\frac{P^{n+1}_{i,j} - P^{n+1}_{i,j-1}}{\Delta x}\right). \quad (12)$$

To numerically calculate the pressure and the velocity components, sequential updating of the eqs. (10), (11) and (12) have been done in the order of increasing i and j. However, an examination of these equations reveal that the values of pressure and velocity components at grid cells placed after the cell at which calculation is being done are required at any time step. For example in eq. (10), to calculate $P^{n+1}_{i,j}$, the updated values of $P^{n+1}_{i+1,j}$ and $P^{n+1}_{i,j+1}$ are required. Here, we have approximated these values at the $n+1$th time step to be equal to their corresponding values at the nth time step. Apart from affecting the convergence rate of the steady-state pressure and velocity values, this approximation does not affect the final distribution.

Equations for the evolution of the pressure and velocity components are as follows:

$$P^{n+1}_{i,j} = \frac{1}{4}\left[P^{n+1}_{i-1,j} + P^{n}_{i+1,j} + P^{n+1}_{i,j-1} + P^{n}_{i,j+1} - \frac{\rho\Delta x}{\Delta t}\left(u^{n}_{i+\frac{1}{2},j} - u^{n}_{i-\frac{1}{2},j} + v^{n}_{i,j+\frac{1}{2}} - v^{n}_{i,j-\frac{1}{2}}\right)\right], \quad (13)$$

$$u^{n+1}_{i+\frac{1}{2},j} = \frac{1}{4+\gamma}\left[u^{n}_{i+\frac{1}{2},j+1} + u^{n+1}_{i-\frac{1}{2},j} + u^{n}_{i+\frac{3}{2},j} + u^{n+1}_{i+\frac{1}{2},j-1} + \gamma u^{n+1}_{i+\frac{1}{2},j} - \frac{\Delta x}{\mu}\left(P^{n+1}_{i+1,j} - P^{n+1}_{i,j}\right)\right], \quad (14)$$

$$v^{n+1}_{i,j-\frac{1}{2}} = \frac{1}{4+\gamma}\left[v^{n}_{i,j+\frac{1}{2}} + v^{n+1}_{i-1,j-\frac{1}{2}} + \gamma v^{n+1}_{i,j-\frac{1}{2}} + v^{n+1}_{i,j-\frac{3}{2}} + v^{n}_{i+1,j-\frac{1}{2}} - \frac{\Delta x}{\mu}\left(P^{n+1}_{i,j} - P^{n+1}_{i,j-1}\right)\right], \quad (15)$$

where

$$\gamma = \frac{(\Delta x)^2}{\eta\Delta t}.$$

Equations (13), (14) and (15) are applied to each of the grids lying within the pore channel. The above equations are solved by Gauss–Seidel's iterative method. If there are n number of cells in a row, there are $(n+1)$ number of u s to solve. Similarly the number of v s to solve is one more than the number of cells in that column.The boundary conditions required for solving the equations are

(1) $u = v = 0$ at the pore–rock boundary.

(2) The pressures at inlet and outlet of the pore channel are specified as desired.

(3) When the eqs. (10), (11) and (12) are applied to grid-cells having at least one face coinciding with the physical boundary of the system, terms outside the flow region appear, which do not exist physically. Here, we superimpose imaginary nodes outside the boundary, often referred to as *image-grids* (Aziz & Settari 1979).

The rigid interface between pore and matrix exhibit a no-slip boundary condition. Let v' be the y component of the velocity beyond a vertical rigid wall in the imaginary grid. For *no-slip* condition at the boundary, $v' = -v_1$, where v_1 is the y component of the velocity in the pore grid. Also since $\vec{\nabla}.\vec{V} = 0$ in the fluid cell, it follows that for $\vec{\nabla}.\vec{V}' = 0$ to vanish in the imaginary cell, $u' = u_1$. The left-hand figure in Fig. 3 summarizes the boundary condition across the vertical wall. Here, u_1 is the $\times$ component of the velocity in the fluid cell (Harlow & Welch 1965).

Analogous boundary conditions for velocity are applied at a horizontal wall (right hand figure in Fig. 3). To summarize, the velocity boundary conditions at no-flow boundaries—the normal velocity component remains the same, while the tangential velocity reverses.

(4) The consistency of the boundary condition for P with the vanishing of the normal velocities on the boundary should be maintained.

Substitution of the velocity boundary condition as enlisted in (3) in eqs. (14) and (15) yield the following:

$$P'^{n+1} = P^{n+1}_1 \pm 2\mu\frac{u^{n+1}_1}{\Delta x}, \quad (16)$$

$$P'^{n+1} = P^{n+1}_1 \pm 2\mu\frac{v^{n+1}_1}{\Delta x}, \quad (17)$$

where P_1 is the pressure at the centre of the pore-cell, P' is the pressure at the centre of the adjacent imaginary cell, "+" sign is for fluid to the left of the wall and "−" for fluid to the right.

Equations (16) and (17) indicate that to calculate pressure in the imaginary cells, we need to know the velocity in the fluid cell at the same time step.To circumvent this problem and simplify our numerical computations, we approximate velocities to be vanishing near the walls ($u_1 = 0, v_1 = 0$) only when an expression for P′ needs to be found. This yields $P' = P_1$ which is the pressure in the fluid cell. Physically the result implies that the pressure gradient across a no-flow boundary should be zero which can be easily seen from Darcy's equation (Aziz & Settari 1979).

(5) We put some restrictions at the inlets/outlets to define the mode in which the fluid should enter and leave the pore-channel. Imaginary cells are superimposed adjacent to the pore-cells at the inlets and outlets outside the pore channel. We assume the fluid flows normally to the inlets/outlets, which allows us to equate the tangential velocity component in the imaginary cell to zero. Hence, to satisfy continuity in the imaginary cell, the normal component has to remain unchanged within the cell.

3.1 Validation of the model

The u and v values are calculated on the faces of the grid-cells; for example at $(i+\frac{1}{2}, j)$ and $(i, j-\frac{1}{2})$, respectively. The pressure and velocity of the grid are stored in a double dimensional array whose arguments refer to the i and j positions, respectively. Since these arguments have to be of the integer data type, we superpose two different matrices of grid-cells; one for solving the us and the other for solving the vs. The one for us is such that the point $(i+\frac{1}{2}, j)$ which was on the face of a cell in the original grid structure is the centre of a cell in the first new grid structure. Similarly for v s, the point $(i, j-\frac{1}{2})$, which was on the face of a cell in the original grid structure serves as the centre of a cell in the second new grid structure (Fig. 4).

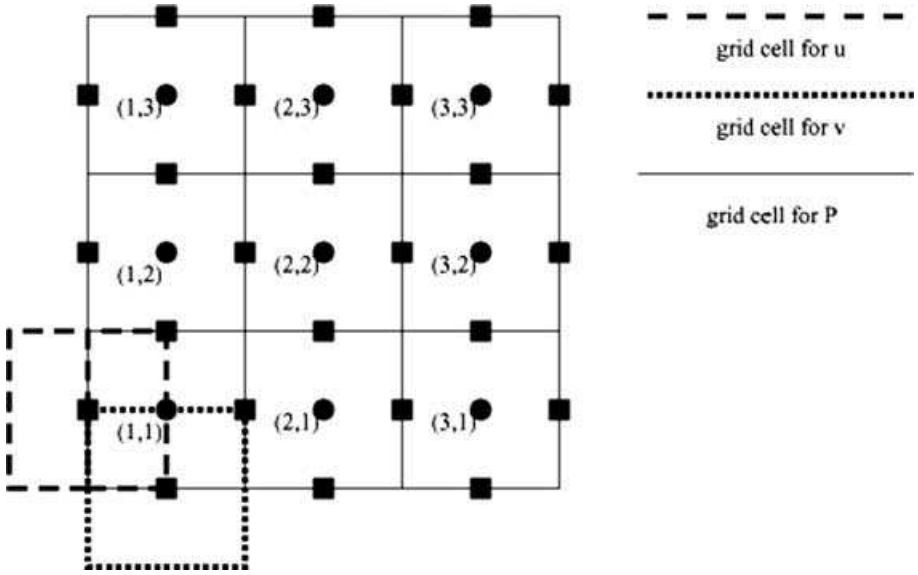

Figure 4. The relative placements of the grids for pressure P and velocity components for x- and y- directions are illustrated.

Hence the equations, which are fed to the computer system appear as

$$P_{i,j}^{n+1} = \frac{1}{4}\Big[P_{i-1,j}^{n+1} + P_{i+1,j}^{n} + P_{i,j-1}^{n+1} + P_{i,j+1}^{n} - \frac{\rho\Delta x}{\Delta t}\left(u_{i+1,j}^{n} - u_{i,j}^{n} + v_{i,j+1}^{n} - v_{i,j}^{n}\right)\Big], \tag{18}$$

$$u_{i,j}^{n+1} = \frac{1}{4+\gamma}\Big[u_{i,j+1}^{n} + u_{i-1,j}^{n+1} + u_{i+1,j}^{n} + u_{i,j-1}^{n+1} + \gamma u_{i,j}^{n+1} - \frac{\Delta x}{\mu}\left(P_{i,j}^{n+1} - P_{i-1j}^{n+1}\right)\Big], \tag{19}$$

$$v_{i,j}^{n+1} = \frac{1}{4+\gamma}\Big[v_{i,j+1}^{n} + v_{i-1,j}^{n+1} + \gamma v_{i,j}^{n+1} + v_{i,j-1}^{n+1} + v_{i+1,j}^{n} - \frac{\Delta x}{\mu}\left(P_{i,j}^{n+1} - P_{i,j-1}^{n+1}\right)\Big]. \tag{20}$$

We have used $\varepsilon = 0.001$, $\mu = 2$ cp, $\rho = 0.8$ g/cc, $\Delta x = 10^{-2}$ cm, $\Delta P = 1$ dyne, $\Delta t = 0.25 \times 10^{-4}$ s.

The proper choice of Δx and Δt is very crucial. Decreasing Δx and Δt as far as possible can lead to better resolution, but keeping in mind the limitations of computer resources, we chose the above values.

Apart from calculation of pressure and velocity distribution, the program developed also monitors the difference in the amount of mass flowing in and out of the system. Ideally, it should be zero, since we have assumed the fluid to be incompressible, but for the various approximations some errors creep in and the difference does not vanish identically. We have considered only those solutions where the error in mass conservation $\leq$2.5 per cent. To test the accuracy of our simulated model, we compare the results obtained through simulation with the analytical solution of fluid flow on a plane rectangular geometry.

The areal flow rate Q can be formulated as

$$Q = \frac{h^3}{12\mu}\frac{\partial P}{\partial x}, \tag{21}$$

where h is the width of the rectangular pore channel and $\frac{\partial P}{\partial x}$ is the pressure gradient applied across the length of the pore channel. Comparing the average velocity calculated from eq. (21) and from the simulation is one way to test the efficacy of the procedure followed.

Usually, the minimum channel width considered to give a parabolic velocity profile for Poiseuille flow is 8, we propose to work with minimum channel width 4, to reduce computer requirement. To show that this does not change the qualitative nature of the results, we calculate the average velocity for a straight channel of 4 and 8 cells width.

For a cell 4 cells wide in a system of size 128, we have

$$(v_{sim})_{av} = 0.00560 \quad \text{and} \quad (v_{th})_{av} = 0.00529$$

For a channel 8 cells wide in a 256 sized system, the same results are

$$(v_{sim})_{av} = 0.00969 \quad \text{and} \quad (v_{th})_{av} = 0.01049.$$

Here, v_{sim} represents the simulated result and v_{th} the result calculated from eq. (21).

We have also tested the velocity distribution on a branched channel for eight times (in a 256 size sample) and four times (in a 128 size sample) magnification of the RBBDM unit cell. The results, illustrated in Fig. 5, show that the distribution is very similar in the two cases. The right-hand side branch in the figure is of narrowest possible width. The percentage error in mass conservation in the two cases is .00065 per cent for system size 256 and.0023 per cent for system size 128.

3.2 Results for pressure and velocity distribution before diagenesis

Once the steady-state fluid flow is established through the sample, the permeability is determined from Darcy's law. We assume that unit pressure difference is imposed across the sample and calculate the flux, using the steady-state flow velocities. We have calculated the permeability (κ) in 200 configurations for each value of p ranging

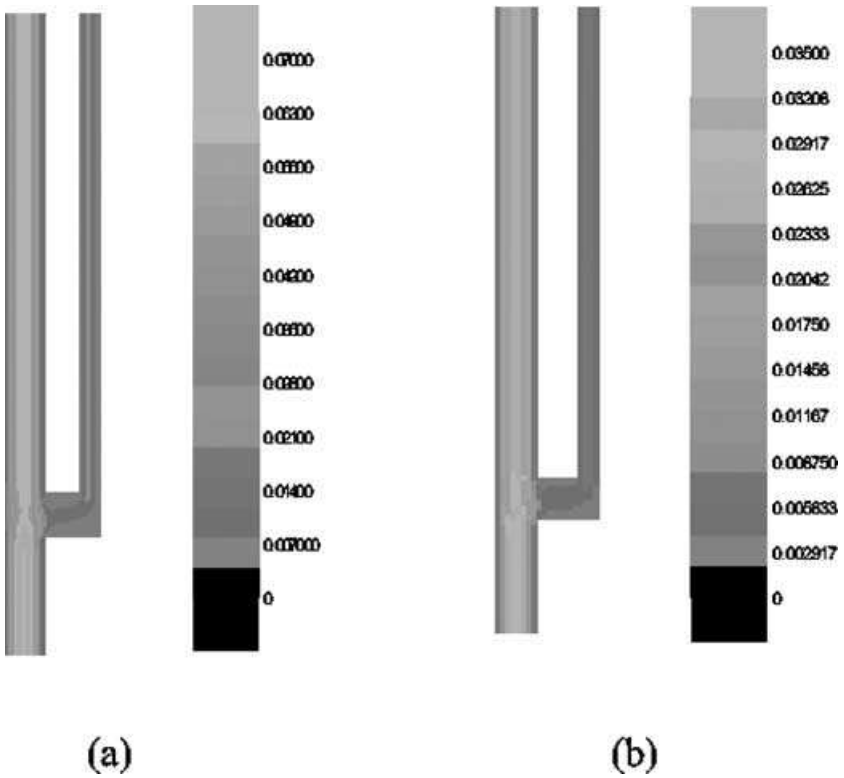

Figure 5. Test results are shown for (a) 8 × 8 and (b) 4 × 4 magnification of the units in RBBDM. (a) and (b) show the velocity distribution obtained in a branched channel with the same geometry for eight times magnification in a system of size 256 and four times in a system of size 128, respectively. The narrow branch on the right has the minimum pore width possible in our system (i.e. eight cells in (a) and four cells in (b)). Velocity distributions obtained are essentially similar.

from 0 to 0.9, where sample spanning pore channels were formed. We chose 100 configurations with one sample spanning channel and 100 with two channels. Configurations with more than two channels were not detected in any trial. Since the system studied is below the percolation threshold, we had to run more than 800 trial configurations to get 100 configurations having a single connected channel. More than 13000 trial configurations had to be run to choose 100 having two connected channels. In every case, we generated a 128 × 100 sample from which a 32 × 32 sample was selected after the porosity had stabilized. A sample larger than the system to be studied has to be generated to avoid substrate effects, this is discussed in detail in Dutta & Tarafdar (2003).

The 32 × 32 sample was magnified to 128 × 128 sample as discussed previously and simulation was carried out on it. Pressure and velocity distributions have been determined for all the 200 samples for each value of porosity. Next, we subject the sample generated to diagenesis according to the prescription detailed below.

4 DIAGENESIS

The restructuring of the pore space formed by deposition and compaction is termed *diagenesis*. Diagenesis takes place at a molecular level, whereas the sand grains deposited are typically of the order of microns. Diagenesis consists of two processes (i) the deposition on the surface or interstices between the grains from chemical reactions in the pore-filling fluids and (ii) the dissolution of material from the grains. The first process decreases the total pore space, whereas the second increases it. Usually it is the deposition or cementation which dominates, so the overall porosity decreases with time due to diagenesis (Pettijohn 1984). There is no unique relation between porosity and permeability, materials having same porosity may have very different permeability. The pore geometry and connectivity are crucial factors in determining permeability. The Kozeny–Carman relation and its modifications (Dullien 1992) are attempts to define connectivity. The specific surface area, i.e. the area of the pore–grain interface per unit volume is a factor in this formulation. Attempts have been made to calculate permeability variation with porosity for the BBDM (Dasgupta *et al*. 2000; Tarafdar & Roy 1998) using the Kozeny relation. However, if the flow velocity is calculated numerically for a specific configuration of the BBDM or RBBDM, the permeability for that configuration can be determined directly, without resorting to approximate models.

In the present work, our interest is to find the change in permeability with diagenesis. So we first simulate the pore structure using RBBDM, then calculate the flow velocity distribution and hence permeability for configurations with one or more sample spanning clusters. Next, we simulate diagenesis on those specific configurations and finally recalculate the flow velocity, to find the change due to diagenesis.

In simulating diagenesis, we have to agree upon a realistic algorithm. It is reasonable to assume that deposition will occur at points in the pore structure where the fluid is stagnant, i.e. flow velocity is very low. We may expect erosion of projections on the pore walls formed due to the stochastic ballistic deposition of grains. The original 'grains' in the RBBDM have been already magnified 4 × 4 times to facilitate numerical solution of eqs. (10)–(12). So each of

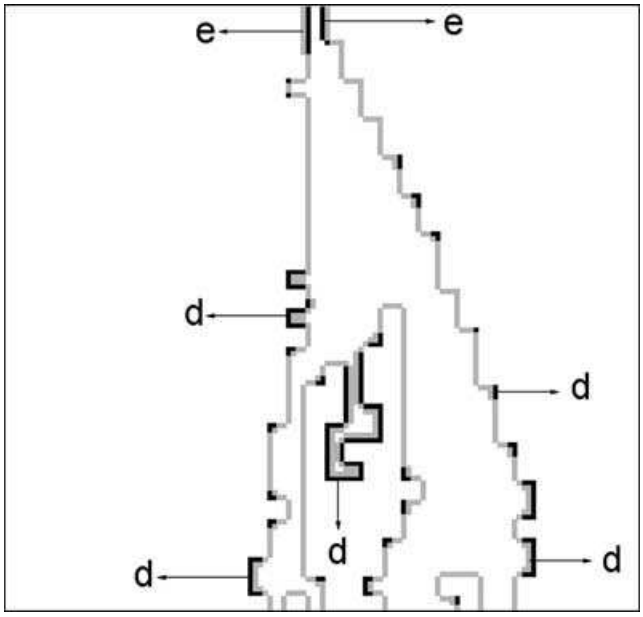

Figure 6. The detailed map of a typical connected channel, flow is upward, from the bottom of the figure. The light grey outline shows the pore–rock interface. Heavy black lines show the changes due to diagenesis. The black lines within the pore channel represent erosion, marked by 'e', and the lines outside show deposition, some are marked 'd'. The deposition events clearly outnumber erosion, but in this channel, erosion occurring at the mouth of the channel increases permeability by 89 per cent.

the sites on the new mesh represent an area 16 times smaller than the small grain size in the RBBDM. We deposit or erode these new sites in our simulated 'diagenesis', so diagenesis is at a smaller level than the grain size, as it should be. We specify a minimum velocity $v_{\min}$ and deposit cementing material at all pore sites with velocity lower than this. We specify also a maximum velocity $v_{\max}$ and erode neighboring rock sites with velocities higher than that. Our choices of these limits are not unique but serve the purpose of illustrating the outcome of a possible physical diagenetic process, which is the aim of this work.

After generating the velocity distribution for 200 spanning configurations, inspection of the velocity profile at all sites at the pore–matrix boundary, reveal the minimum velocity range between 10^{-13} to 10^{-5} cms^{-1} and maximum velocity of the order 10^{-2} cms^{-1}. We have selected deposition sites as those having a velocity lower than 0.00014 cms^{-1}($v_{\min}$). The erosion sites are chosen as those having velocities greater than 0.02 cm s^{-1} ($v_{\max}$). The net number of deposition and erosion events is recorded. After the 'diagenesis' according to the prescription just described, the permeability is calculated again using the same procedure described for the original channel. Effect of diagenesis on permeability is studied for a range of p varying from 0 to 0.9, which corresponds to initial porosities in the range 0.25 to 0.34.

4.1 Calculation of permeability change with diagenesis

Now we subject the sample to diagenesis. The vacant sites within the pore channel, where the fluid velocity is below $v_{\min}$ are filled up due to cementation and the rock sites adjacent to pore sites with velocity above $v_{\max}$ are eroded. This simplified algorithm for diagenesis results in change of the pore channel morphology. Typical changes in a single pore channel for $p = 0.2$ are illustrated in Fig. 6. Figs. 7(a) and 7(b) show the effect of diagenesis on the velocity distribution. With the diagenesis prescription described, we find that the predominating process is deposition, which clearly dominates over erosion. In fact, in none of the samples does erosion exceed cementation. Table 1 shows the percentage of configurations where erosion occurred at different p for samples with single and double sample spanning pore channels. In all cases however, including these, the number of deposition events exceeded erosion events. It is evident that our simulated diagenesis reduces porosity on the average.

We repeat the flow simulation procedure in the post-diagenesis structures and calculate the change in permeability. Most of the samples show a very small (less than 1 per cent) *decrease* in permeability, which is understandable as cementation is the dominating process. However, very surprisingly, a significant number show a significant increase in permeability, in spite of overall cementation, which is close to 100 per cent in some cases. The percentage increase in permeability for the samples where increase was observed, is shown in Fig. 8 for different p. The channel geometry and its change after diagenesis for a few cases with high increase in κ, was scrutinized individually. We found that in each case the erosion, though less than the deposition, occurs at the pore inlet, outlet or a constriction on the fluid-carrying branch of the channel backbone. Even a few cementing grains eroded from the mouth of the channel can cause a striking increase of permeability. Erosion at any other position would not produce a significant change, but our algorithm introduces erosion almost exclusively at such sites, so wherever there was erosion, permeability increased.

Since it is not possible to map explicitly all the channels of interest, we constructed an hourglass-shaped channel, with a narrow constriction at the centre and subjected it to diagenesis. Erosion was observed at the constriction, as expected and κ increased by 12 per cent, in this case.

The deposition events, though higher in number, always occur at sites, usually dead ends, which are avoided by the moving fluid anyway.

The average permeability (κ) before diagenesis and the average percentage change in permeability after diagenesis ($\Delta\kappa$) for all values of p are shown in Fig. 9. The values of κ may be compared with permeability for real rocks which have a wide variation from 0.1 to >50 cm^2. Our values are in the range of porous cemented rocks, aleurites and sandstones (10^{-2}cm^2) (Kobranova 1989). Of course, this being a 2-D simulation, numerical values should not be taken too seriously. It is interesting to note that κ and $\Delta\kappa$, both have a maximum close to $p = 0.5$. In RBBDM, the porosity also has a maximum at $p = 0.5$, this is shown in the inset in Fig. 9.

6 DISCUSSION

We have proposed an algorithm to mimic natural generation and diagenesis of sedimentary rocks.

In the 3-D RBBDM, the sand grains are rectangular parallelepiped in shape. Most reconstruction models consider spherical (Manwart *et al*. 2000; Øren & Bakke 2002) grains or ellipsoidal grains with different aspect ratio (Coelho *et al*. 1997). However, scrutiny of thin section images (see e.g. Øren & Bakke 2002) shows that sand grains are in fact significantly angular in shape. This is not surprising, since the basic units are aggregates of poly-crystals. We argue that a spherical or ellipsoidal grain approximation is as drastic an oversimplification as the present cubic or rectangular grain model (RBBDM). The two approaches represent two extreme pictures. While the ellipsoidal grains give point contacts, rather than the flat surface contacts of RBBDM, the corners and sharp angular

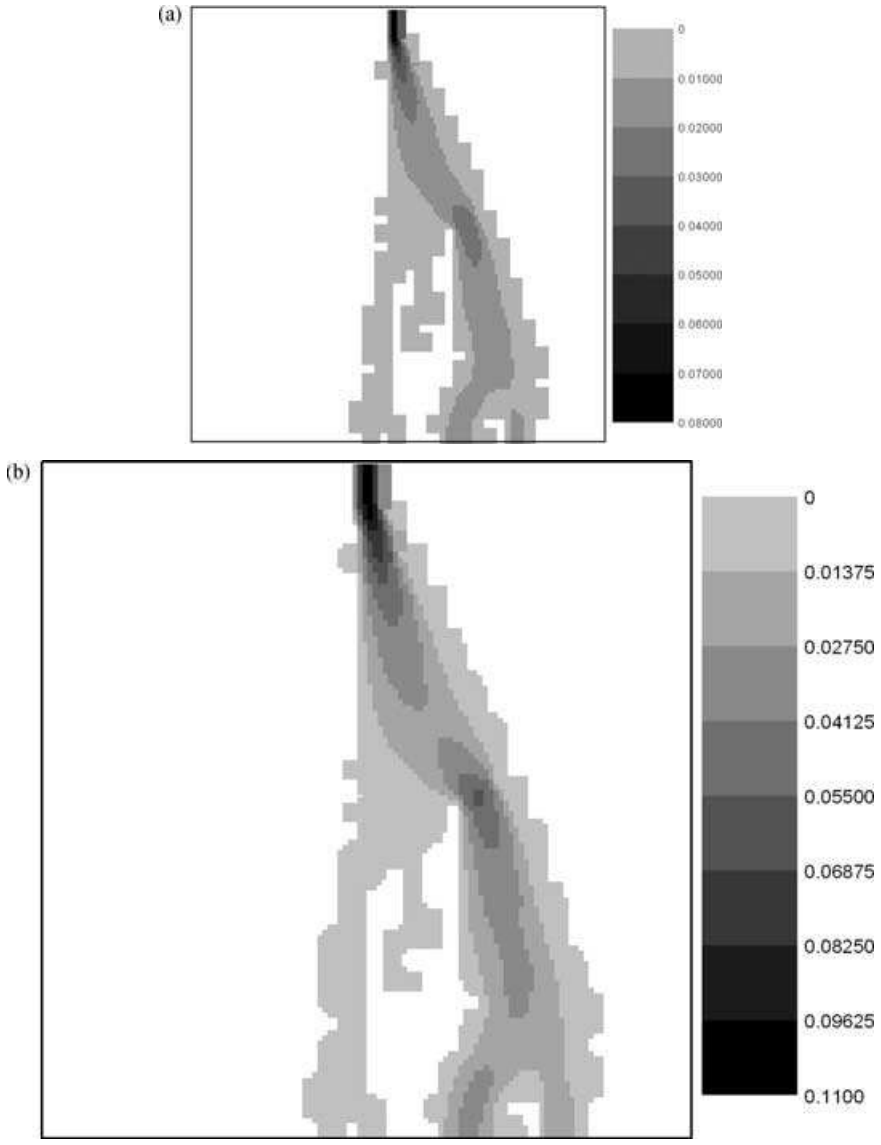

Figure 7. (a) We show the velocity distribution before diagenesis. The variation in velocity shown in the code is in cm sec^{-1}. (b) We show the velocity distribution after diagenesis. Erosion and deposition at the positions shown in Fig. 6 lead to increased flow under the same pressure gradient as in (7a). Permeability has increased by 89 per cent. The variation in velocity shown in the code is in cm sec^{-1}.

Table 1. Percentage of configurations in which erosion occurred.

$p \rightarrow$	0.0	0.2	0.4	0.5	0.6	0.8	0.9
Single channel E(1)	27	20	19	26	14	10	6
Double channel E(2)	33	47	40	38	40	28	9

Notes: Percentage of configurations with erosion, E(n) = number of configurations with 'n' connected channels/ total number of configurations. For p close to 1, erosion is very rare, the channels here are mainly narrow straight columns.

structures produce more realistic pressure distributions than artificially rounded grains in RBBDM. Pittman 1979, discusses the importance of angularity in making grains more susceptible to pressure solution. Exact point contact between spheres is not very realistic either, and compaction has to be introduced to expand the contact area. We must further keep in mind that, all said and done, we finally resort to finite element analysis to calculate transport properties and replace the simulated rock structure by a mesh of points. Unless a very fine mesh can be used, at a tremendous expense of computer memory and time, the detailed contours of the square or round grains hardly make a difference to the final results. What really matters is the connectivity and gross structure of the pore space.

Our treatment of diagenesis is purely from a physical point of view, we have not taken into account the chemistry behind the grain growth and dissolution processes. This is no doubt an oversimplification, but we have taken into account the role of the flow process in shaping the tortuous pore channels during mechanical deposition. The usual approach is to allow growth of a cementing layer, either uniformly on the grain surfaces, or specifically towards the pore volume or in the pore throat (Jin *et al*. 2004; Øren & Bakke 2003; Øren & Bakke 2002).

We consider moreover, flow under a pressure gradient, rather than molecular diffusion. This is reasonable, since we are finally interested in the permeability, with the implication that fluids are

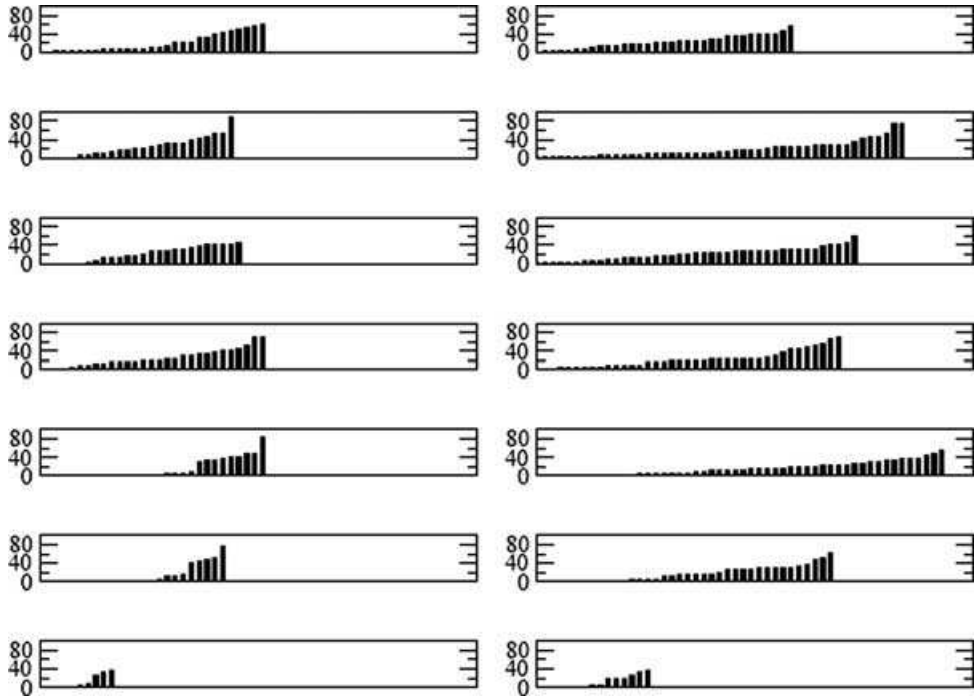

Figure 8. Here, we show the percentage increase in permeability in the channels wherever it has increased. Each bar denotes one configuration where κ increased, its height shows the percentage increase for that particular configuration. Configurations further left to the bars shown have a non-zero height, too small to be visible. The left column correspond to results for samples with a single spanning channel, the right-hand side graphs are the same results for samples with two spanning channels. Diagrams from top to bottom correspond to $p = 0.0$, 0.2, 0.4, 0.5, 0.6, 0.8 and 0.9, respectively.

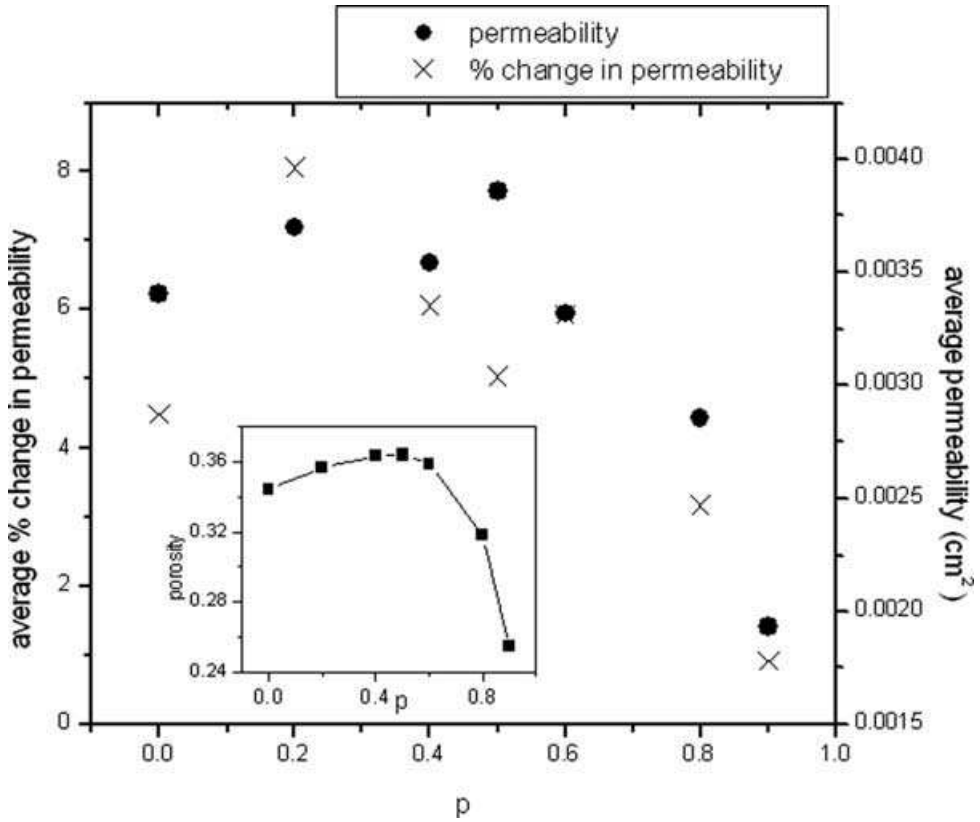

Figure 9. The average permeability (κ) (circular symbol) and change in permeability ($\Delta\kappa$) (cross) due to diagenesis, for different p. Note that both quantities are maximum in the interval $p = 0.2$ to 0.6. The corresponding porosities, before diagenesis, are also shown in the inset. The level of diagenesis we have applied here does not change the porosity significantly.

actually flowing through the pore space, under a finite pressure gradient. So, according to our approach, this is the condition under which diagenesis is reshaping the pore structure. (Hartmann *et al*. 2000) emphasize the importance of hydrological flow in channel reshaping and suggest that the effect of diffusion in transporting the reacting species is weaker. According to Hartmann *et al*., rapid flow promotes leaching while a slower flux preferentially enhances cementation. This is in accordance with our approach. The relative effects of advection and molecular diffusion on channel reshaping is also studied by (Detwiler *et al*. 2003) who discuss experiments and simulation on the problem of erosion at different Peclet numbers. Diffusion may play a significant role where the fluid is almost stagnant, but we consider here the other limiting case where the channel length typically exceeds diffusion length and advection dominates (see also Lobkovsky *et al*. 2005). A study with competing diffusion and advection is in progress and we hope to report the results soon.

Our prescription for diagenesis produces both erosion and cementation, with cementation dominating. However, reduction in permeability due to the decrease in porosity is insignificantly small, though it is observed in a larger number of cases. In the fewer instances where there is permeability *enhancement*, the percentage increase is in comparison, significantly large. So, on the average, we find the net result of diagenesis to be increased fluid flow. However, we have yet to study the effect of variation of the limits $v_{\min}$ and $v_{\max,}$ and repeat the diagenetic process successively, these may change results considerably. Most importantly, we must extend the treatment to 3-D, before we can actually compare with field data. At present, we may only remark that both cementation and deposition occur in diagenesis. The effect on permeability may also be positive or negative for specific cases. So we suggest that our simple algorithm may be adapted to explain these cases on varying the parameters controlling diagensis. This work is a preliminary study in a 2-D version of the original 3-D RBBDM. We expect to get more reliable results from simulations in 3-D, since connectivity and flow properties are quite different in 2- and 3-D . However, considering the many-fold increase in computer memory and time that a 3-D simulation will require this initial 2-D study seems worthwhile. Another difference of our simulation with the real situation is that in reality, length scales for diagenesis and deposition are quite different. The sand grains deposited are several orders of magnitude larger than the typical size of cement deposits. In our model this difference is only 16 times, being the difference between the smallest unit in RBBDM generation and that for the diagenetic process. We hope to report more detailed studies in future with modifications along these lines.

ACKNOWLEDGMENTS

SS is grateful to CSIR for the grant of a research fellowship. The computation has been carried out using the IBM P690 at the Mobile Computing Center, JU, the authors thank Nandini Mukherji and her group for their help.

REFERENCES

Aziz, K. & Settari, A., 1979. *Petroleum Reservoir Simulation*, Applied Science Publishers Ltd., London.

Coelho D., Thovert J.-F. & Adler P.M., 1997. Geometrical and transport properties of random packings of spherical and aspherical particles, *Phys. Rev. E,* **55,** 1959–1978.

Dasgupta, R., Roy, S. & Tarafdar, S., 2000. Correlation between porosity, conductivity and permeability of sedimentary rocks — a ballistic deposition model, *Physica A,* **275,** 22.

Detwiler R.L., Rglass R.J. & Bourcier W.L., 2003. Experimental observation of fracture dissolution: the role of Peclet number on evolving aperture variability, *Geophys. Res. Lett.,* **30,** 1648–1652.

Dullien, F.A.L., 1992. *Porous Media: Fluid Transport and Pore Structure,* Academic Press, San Diego.

Dutta, T. & Tarafdar, S., 2003. Fractal pore structure of sedimentary rocks-simulation by ballistic deposition, *J. Geophys. Res.,* **108,** 2062

Dutta, T. & Tarafdar, S., 2005. Simulation of sedimentary rocks by ballistic deposition, *Proc. 9th World Mtlticonference on Systemics, cybernetics and informatics,* Orlando, July 10–13, Florida, 151 p.

Harlow, F.H. & Welch, J.E., 1965. Numerical calculation of time-dependent viscous incompressible flow of fluid with free surface, *The Physics of Fluids,* **8,** 2182–2189.

Hartmann, D.J., Beaumont, E.A. & Coalson, E., 2000. Predicting sandstone reservoir system quality and example of petrophysical evaluation, Search and discovery article #40005, http://www.searchanddiscovery.net/documents/beaumont/index.htm

Hoshen, J. & Kopelman, R., 1976. Percolation and cluster distribution. I. Cluster multiple labeling technique and critical concentration algorithm, *Phys. Rev. B,* **14,** 3438.

Jin, G., Patzek, T.W. & Silin, D.B., 2004. Direct prediction of the absolute permeability of unconsolidated and consolidated reservoir rock, *Soc. Petro. Eng.,* Paper 90084.

Kobranova, V.N., 1989. *Petrophysics,* Mir Publishers, Union of Soviet Socialist Republics.

Lobkovsky A.E., Smith B., Kudrolli A. & Rothman D.H., 2005. Dynamics of channel incision in a granular bed driven by subsurface water flow, arXiv:cond-mat/0505352

Manwart, C., Torquato, S. & Hilfer, R., 2000. Stochastic reconstruction of sandstones, *Phys. Rev. E,* **62,** 893.

Øren, P.-E. & Bakke, S., 2002. Process based reconstruction of sandstones and prediction of transport properties, *Trans. Porous Media,* **46,** 311–343.

Øren, P.-E. & Bakke, S., 2003, Reconstruction of Berea sandstone and pore-scale modelling of wettability effects, *J. Petro. Sci. Engg.,* **39,** 177–199.

Pape, H., Clauser, C. & Iffland, J., 1999. Variation of permeability with porosity in sandstone diagenesis interpreted with fractal pore space model, *Geophysics,* **64,** 1447–1460.

Pettijohn, F.J., 1984. *Sedimentary Rocks,* Harper & Row Publishers, Inc., U.S.A.

Pittman E.D., 1979. Sandstone Diagenesis, *Ann. Rev. Earth Planet. Sci.,* **7,** 39–62.

Sarkar, S., Toksöz, M.N. & Burn, D.R., 2004. *Fluid Flow Modelling in Fractures,* MIT Earth Resources Laboratory Industry Consortium Meeting.

Schwartz, L.M., Martys, N., Bentz, D. P., Garboczi, E.J. & Torquato, S., 1993. Cross-property relations and permeability estimation in model porous media, *Phys. Rev. E,* **48,** 4584–4591.

Stauffer, D. & Aharony, A., 1994. *Introduction to percolation theory,* Burgess Science Press, Basingstoke, Great Britain.

Tarafdar, S. & Roy, S., 1998. A growth model for porous sedimentary rocks, *Physica B,* **254,** 28.